PNAS RESEARCH ARTICLE | GENETICS

Role of the bicarbonate transporter SLC4γ in stony-coral skeleton formation and evolution

Amanda I. Tinoco[a,b], Lorna M. Y. Mitchison-Field[a,c], Jacob Bradford[d,e], Christian Renicke[c], Dimitri Perrin[d,e], Line K. Bay[f], John R. Pringle[c], and Phillip A. Cleves[a,b,c,1]

Edited by Nancy Knowlton, Smithsonian Institution, Washington, DC; received September 26, 2022; accepted April 26, 2023

Coral reefs are highly diverse ecosystems of immense ecological, economic, and aesthetic importance built on the calcium-carbonate-based skeletons of stony corals. The formation of these skeletons is threatened by increasing ocean temperatures and acidification, and a deeper understanding of the molecular mechanisms involved may assist efforts to mitigate the effects of such anthropogenic stressors. In this study, we focused on the role of the predicted bicarbonate transporter SLC4γ, which was suggested in previous studies to be a product of gene duplication and to have a role in coral-skeleton formation. Our comparative-genomics study using 30 coral species and 15 outgroups indicates that SLC4γ is present throughout the stony corals, but not in their non-skeleton-forming relatives, and apparently arose by gene duplication at the onset of stony-coral evolution. Our expression studies show that *SLC4γ*, but not the closely related and apparently ancestral *SLC4β*, is highly upregulated during coral development coincident with the onset of skeleton deposition. Moreover, we show that juvenile coral polyps carrying CRISPR/Cas9-induced mutations in *SLC4γ* are defective in skeleton formation, with the severity of the defect in individual animals correlated with their frequencies of *SLC4γ* mutations. Taken together, the results suggest that the evolution of the stony corals involved the neofunctionalization of the newly arisen SLC4γ for a unique role in the provision of concentrated bicarbonate for calcium-carbonate deposition. The results also demonstrate the feasibility of reverse-genetic studies of ecologically important traits in adult corals.

Acropora millepora | genome editing | gene duplication | neofunctionalization | CRISPR/Cas9

Significance

Coral reefs are biodiversity hotspots that are in decline due to stressors associated with climate change. Thus, a critical research goal is to achieve a deeper understanding of basic coral biology to inform conservation efforts. This goal has been difficult to achieve due to the lack of genetic tools for corals. Here, we used CRISPR/Cas9 mutagenesis to show that a predicted bicarbonate transporter that apparently evolved specifically in the common ancestor of the stony corals is indeed required for formation of the calcium-carbonate skeleton in young coral colonies. The ability to do such genetic analysis in adult corals should now allow critical tests of hypotheses about gene function and the generation of stable, genetically modified lines for research and conservation.

Coral reefs provide the habitat for ~25% of known marine species (1). Stony corals (Order Scleractinia) build these ecosystems by depositing calcium-carbonate-based skeletons, which form the physical structure of the reefs. Scleractinian corals diversified ~240 Mya as primary reef builders, and their ability to biomineralize and form endosymbiotic relationships with dinoflagellate algae presumably played key roles in their adaptive radiation (2–5). Corals are in decline worldwide due to a variety of anthropogenic stressors including those associated with climate change, and future ocean acidification is predicted to further reduce their ability to deposit their reef-building skeletons (6–8). Thus, it is of great importance to understand the molecular mechanisms of coral-skeleton formation and its evolution in order to better predict and possibly mitigate the impacts of ocean acidification (9).

Corals have specialized cells, called calicoblasts, that lie adjacent to the site of calcium-carbonate deposition and are involved in this process, which requires that calcium and bicarbonate ions be concentrated to above their levels in seawater in the space between the calicoblasts and the substrate (10–15). A primary source of the bicarbonate required for calcification appears to be metabolic CO_2 from the highly metabolically active calicoblasts (14–17). This CO_2 is hypothesized to either be converted to bicarbonate by highly expressed carbonic anhydrases in the calicoblasts or diffuse to the site of calcification and be converted to bicarbonate there by extracellular carbonic anhydrases (15, 17–19). However, the relative importance of the passive diffusion of CO_2 versus the transport of bicarbonate is unknown (15, 20–23). Nonetheless, genomic, transcriptomic, and proteomic studies of corals have identified multiple genes that may be involved in the transport of the material required for biomineralization, as well as proteins localized to the skeletal matrix that may contribute to the precipitation of calcium carbonate (2, 9, 18, 24–31). For example, examination of the genomes of two stony corals (*Stylophora pistillata* and *Acropora digitifera*) and a non-biomineralizing relative (the anemone *Nematostella vectensis*) identified five predicted bicarbonate transporters in the SLC4 family (32). Interestingly, this analysis also found that one family member, SLC4γ, was expressed in calicoblasts in *S. pistillata* and appeared to be present only in the stony corals, suggesting that it might supply the bicarbonate required for skeleton formation and thus have contributed to the evolution of this process (32). In

Author contributions: A.I.T., J.R.P., and P.A.C. designed research; A.I.T., L.M.Y.M.-F., L.K.B., and P.A.C. performed research; J.B., C.R., D.P., and P.A.C. contributed new reagents/analytic tools; A.I.T., L.M.Y.M.-F., and P.A.C. analyzed data; L.M.Y.M.-F., J.B., C.R., D.P., and L.K.B. reviewed paper; and A.I.T., L.K.B., J.R.P., and P.A.C. wrote the paper.

The authors declare no competing interest.

This article is a PNAS Direct Submission.

[1]To whom correspondence may be addressed. Email: cleves@carnegiescience.edu.

This article contains supporting information online at https://www.pnas.org/lookup/suppl/doi:10.1073/pnas.2216144120/-/DCSupplemental.

Published June 5, 2023.

contrast, a survey of 20 stony-coral transcriptomes failed to identify *SLC4γ* in seven species, raising doubt about its central role in biomineralization (26). However, these results might be explained by incompleteness of the transcriptomes, the gain and loss of *SLC4γ* in specific stony-coral lineages, or both.

In this study, we used a combination of comparative genomics, gene-expression analysis, and CRISPR/Cas9-induced mutagenesis to provide strong evidence that *SLC4γ* arose at the beginning of stony-coral evolution by tandem gene duplication and was neofunctionalized to play a critical role in calcium-carbonate deposition by juvenile corals.

Results

Evolution of *SLC4γ* by Tandem Gene Duplication and Neofunctionalization. We examined the distribution of *SLC4* family members across 30 stony coral and 15 outgroup genomes (*SI Appendix*, Table S1). Consistent with previous observations, we identified five *SLC4* subfamilies, and a bootstrapped phylogeny demonstrated that *SLC4γ* is most closely related to *SLC4β* (*SI Appendix*, Fig. S1). Although *SLC4β* was found in all cnidarian genomes examined, *SLC4γ* was present only in the stony-coral genomes, and in all of them (Fig. 1*A*), suggesting that *SLC4γ* arose by duplication of *SLC4β* and was subsequently retained broadly in stony corals, in general agreement with previous observations (32).

To investigate the nature of the putative gene duplication, we examined the synteny of orthologous genes around *SLC4β* and found blocks that are conserved across cnidarians (Fig. 1*B* and Dataset S1). Strikingly, where *SLC4γ* is present, it is located on the same scaffold as *SLC4β* in every species but two, *Porites lutea* and *Galaxea fascicularis*, where the *SLC4β* scaffold ends shortly after this gene, probably due to incompleteness of the genome assemblies (Fig. 1*B*). This analysis also revealed a striking difference between the "robust" and "complex" stony corals, phylogenetically distinct groups that have reported differences in skeleton structure (33). In robust corals, *SLC4β* and *SLC4γ* are adjacent, suggesting a tandem duplication, whereas they are several genes apart in complex corals (Fig. 1*B*). Although it is possible that *SLC4β* was duplicated independently in the robust- and complex-coral lineages, the most parsimonious explanation is that

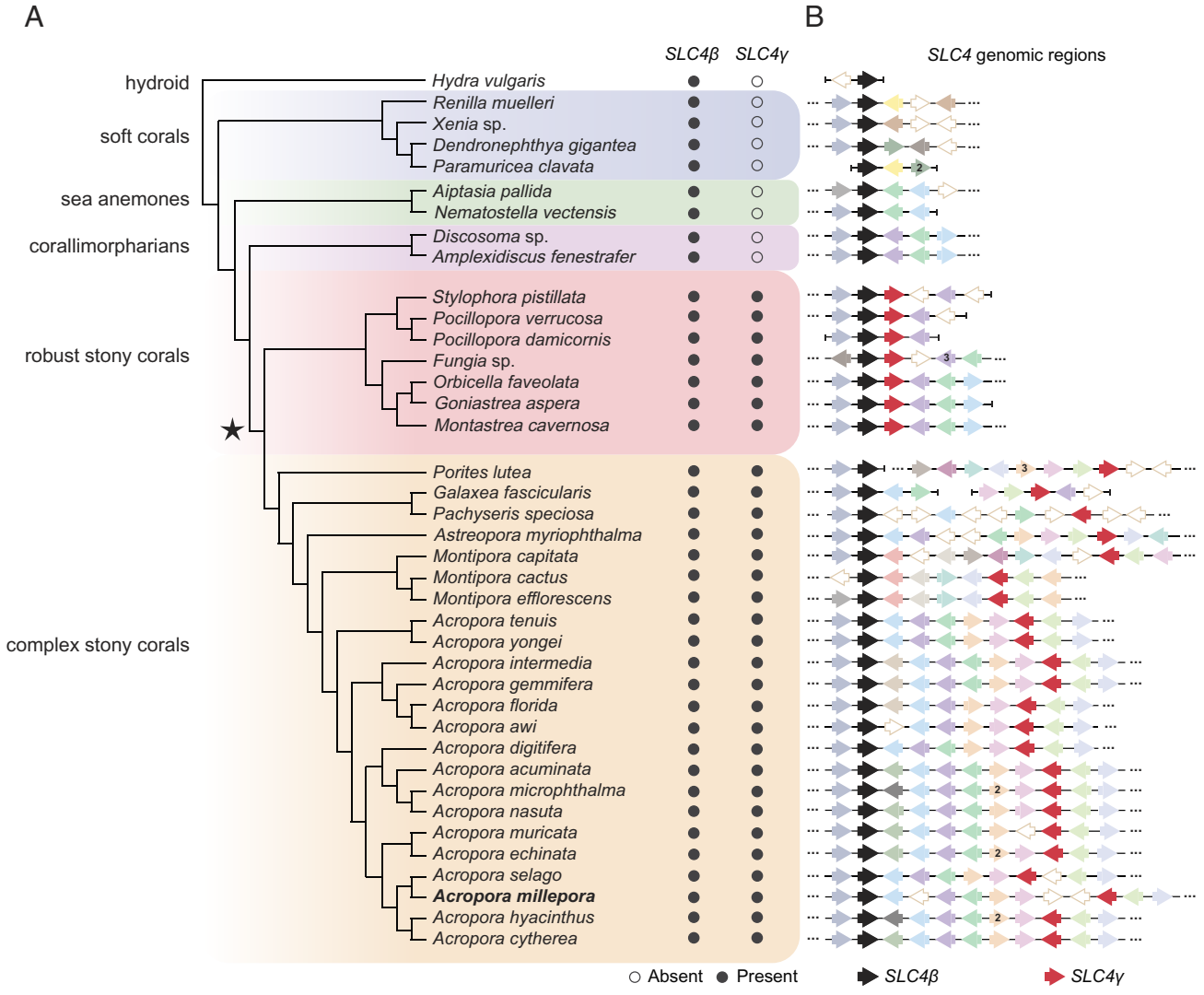

Fig. 1. Evidence that the bicarbonate transporter gene *SLC4γ* arose by local gene duplication in the last common ancestor of stony corals. (*A*) Phylogenetic relationships of 30 stony corals and nine other cnidarians as outgroups, inferred from predicted protein sequences from reference genomes. The presence or absence of *SLC4β* and *SLC4γ* is shown for each species, and the inferred position of the *SLC4β* duplication event is marked with a star. (*B*) Synteny analysis of genes around *SLC4β* (black arrows) and *SLC4γ* (red arrows). Orthologous genes are shown in the same color, and the directions of the arrows mark gene orientations from 5′ to 3′. Empty arrows mark genes present in only that species within this region. Tandem gene repeats are indicated by numbers within the corresponding arrows. Vertical lines mark scaffold ends, and ellipses mark places where the scaffolds continue.

a tandem duplication occurred in the last common ancestor of these groups, followed by specialization of SLC4γ for bicarbonate transport during biomineralization and subsequent genomic rearrangements in the complex-coral lineage. However, the exact pathway of these genomic rearrangements cannot easily be inferred from the synteny patterns in the available modern genomes.

Specific Upregulation of *SLC4γ* at the Beginning of Biomineralization. We used qRT-PCR to evaluate the expression of *SLC4γ* and *SLC4β* during the initiation of skeleton formation by young *Acropora millepora* polyps. We collected gametes during the annual spawning event in northeastern Australia (November, 2019), generated larvae by fertilization in seawater in the Australian Institute for Marine Science's National Sea-Simulator Facility, induced settlement and metamorphosis at 7 d postfertilization by adding chips of crustose coralline algae (CCA) (Fig. 2*A*) (34), and measured *SLC4γ* and *SLC4β* expression at each stage. We found that *SLC4γ* mRNA was indeed upregulated relative to its level in larvae during metamorphosis and the initial formation of septal skeleton (Fig. 2 *B* and *C*). In contrast, *SLC4β* had low expression both in larvae and throughout metamorphosis and the initiation of skeleton formation (Fig. 2*B*). Thus, *SLC4γ* is indeed expressed at a time consistent with a role in biomineralization in juvenile *A. millepora* polyps, and its expression pattern has apparently diverged from that of *SLC4β* since the putative gene duplication occurred.

Loss of Skeleton Formation upon Disruption of *SLC4γ* by CRISPR/Cas9 Mutagenesis. Although the above and previously published data (32) suggest strongly that SLC4γ is a bicarbonate transporter with a role in coral-skeleton formation, this hypothesis has not been tested directly. Until recently, it was not possible to perform such tests in corals due to the lack of genetic tools. However, we showed previously that CRISPR/Cas9 could be used to mutate coral genes (35) and used this technique to demonstrate a role for the heat shock transcription factor (HSF1) in controlling heat tolerance in *A. millepora* larvae (36). To extend this approach to the study of ecologically important traits that develop after the larval stage, such as biomineralization, it is necessary to evaluate possible mutant phenotypes at post-larval developmental stages.

To mutate *A. millepora SLC4γ* (*SI Appendix*, Fig. S1 and Dataset S1), we designed single-guide RNAs (sgRNAs) targeting exons 5 and 10 (Fig. 3*A* and *SI Appendix*, Fig. S2 and Table S2). These positions were chosen to avoid any possible alternative transcription-start sites, minimize potential off-target binding of the sgRNAs, and be early enough in the coding region to disrupt gene function if mutated. During each of the three nights of spawning in November 2019 (treated as independent replicate experiments), we injected freshly fertilized zygotes with a mixture containing a fluorescent injection indicator and either Cas9 protein alone or a mixture of sgRNA1/Cas9 and sgRNA2/Cas9 ribonucleoprotein complexes. For each experiment, we attempted to inject 100 to 200 zygotes per condition (*SI Appendix*, Table S3). Most (62 to 99%) of these zygotes survived and developed normally for 12 h, and 43 to 79% of those injected were positive for the fluorescent marker indicating successful injection (*SI Appendix*, Table S3). Successfully injected individuals were collected at 12 h and used for subsequent analyses of settlement, skeleton formation, and mutation frequency.

For each experiment, we attempted to settle 20 to 60 larvae per condition using CCA at 4 or 5 d postfertilization (*SI Appendix*, Table S4). Most larvae (55 to 83%) settled and metamorphosed seemingly normally in each experiment, with no significant differences between the conditions, indicating that our manipulations did not seriously affect these processes (Fig. 3*B* and *SI Appendix*, Fig. S3 and Table S4, and Dataset S2). We then imaged and quantified radial-septa biomineralization 3 d after settlement using an inverted microscope (Fig. 3 *C*–*F*). Almost all (>90%) of the uninjected and Cas9-only-injected individuals developed normal radial septa in each experiment (Fig. 3 *C*, *D*, and *F* and Dataset S2). In contrast, the sgRNA/Cas9-injected individuals displayed a range of septum-formation defects ranging from a complete lack of visible septa to seemingly normal septa (Fig. 3 *E* and *F* and *SI Appendix*, Fig. S4). Accordingly, we scored each juvenile as Normal, Moderate, or Severe based on the extent of its biomineralization defect. Strikingly, ~85% of the sgRNA/Cas9-injected individuals were scored as having Moderate or Severe defects (Fig. 3 *E* and *F* and Dataset S2). Despite their biomineralization defects, these animals were attached to the substrate and appeared to metamorphose normally, forming mesenteries, mouths, and tentacles (Fig. 3*B* and *SI Appendix*, Fig. S3 and Dataset S2). Thus, the deposition of septal skeleton appears to be a process distinct from larval settlement and early polyp development including the formation of a mouth and tentacles.

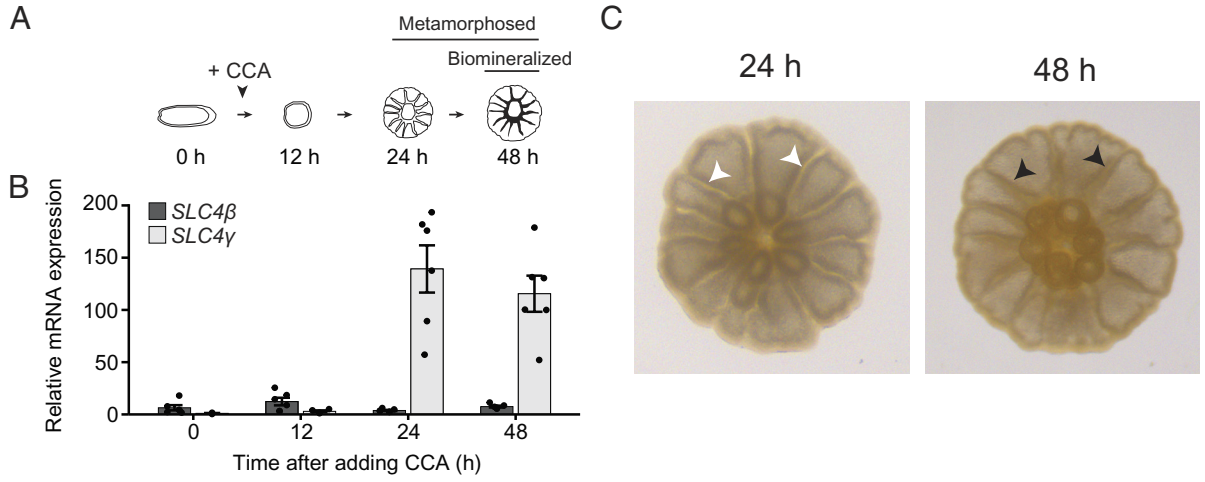

Fig. 2. Evidence that SLC4γ, but not SLC4β, has a role in formation of septal skeleton in juvenile *A. millepora* colonies. (*A*) Design of experiments using CCA as a settlement cue. (*B*) *SLC4β* and *SLC4γ* mRNA levels in individual animals at each time point shown in *A*. Expression values are shown relative to the mean expression of *SLC4γ* at 0 h. Individual measurements are shown (dots) along with means and SEs. (*C*) Representative images of *A. millepora* juveniles at 24 and 48 h after settlement induction. White arrowheads mark tissue gaps where biomineralized septa (black arrowheads) will form.

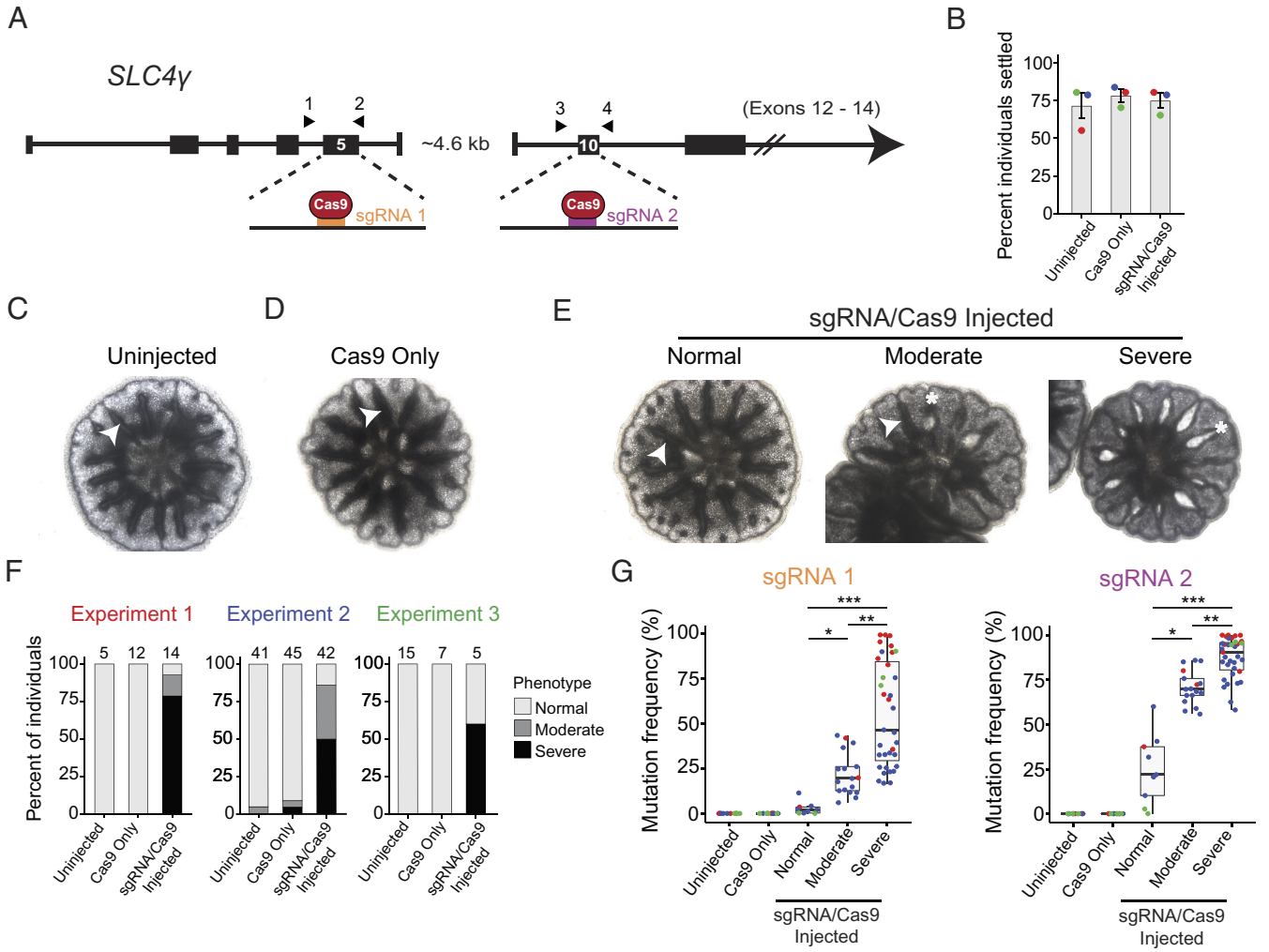

Fig. 3. Reduced skeleton formation in *A. millepora* juveniles with mutations in *SLC4γ*. (*A*) Structure of *SLC4γ* with locations of sgRNA target sites. Seven of the 14 exons are shown (black boxes) with an ~4.6-kb gap between exons 5 and 10. The approximate locations of the target sites for sgRNAs 1 and 2 in exons 5 and 10, respectively, are shown, as are the locations of the primers (arrowheads 1 to 4) used for amplicon sequencing. (*B*) Percentages of uninjected, Cas9-only injected, and sgRNA/Cas9-injected animals in each experiment that settled within 3 d of exposure to CCA. Experiments 1 (red), 2 (blue), and 3 (green) correspond to the three nights of spawning on which zygotes were injected. (*C*–*E*) Representative images of coral juveniles from each condition imaged 3 d after settlement using an inverted microscope. Examples of biomineralized septa (arrowheads) and tissue gaps without biomineralization (asterisks) are indicated. Phenotypes were scored as "Normal" (all septa biomineralized), "Moderate" (one or two septa failed to biomineralize), or "Severe" (three or more septa failed to biomineralize) (see *Materials and Methods* and *SI Appendix*, Fig. S4, for additional details). (*F*) Quantification of biomineralization phenotypes. The numbers of animals per condition within each experiment are shown above the histogram bars. (*G*) Frequencies of mutations at the sgRNA 1 (*Left*) and sgRNA 2 (*Right*) sites for each condition. Boxes denote the first and third quartiles, and the horizontal lines mark the medians. Statistical significances were tested by a Kruskal–Wallis test followed by Dunn's multiple comparison test with a Bonferroni correction (*$P \leq 0.05$; **$P \leq 0.001$; ***$P \leq 0.0001$).

We next asked whether the skeletal defects could be attributed to mutations in *SLC4γ* at either or both of the sgRNA sites. We extracted DNA and generated PCR products spanning each site from 12 uninjected, 12 Cas9-only-injected, and 69 sgRNA/Cas9-injected polyps (Fig. 3*A* and *SI Appendix*, Table S2), and performed high-throughput amplicon sequencing of these products to quantify the mutation frequencies in each individual. No mutations were detected in any of the uninjected or Cas9-only-injected animals (Dataset S2). In contrast, nearly all sgRNA/Cas9-injected corals (68/69) had mutations at either one or both sgRNA sites (Fig. 3*G* and Dataset S2). The frequencies of mutations differed between the two sites, with on average ~39% and ~75% of *SLC4γ* gene copies mutated by sgRNA1 and sgRNA2, respectively. As also seen previously (35, 36), the mutant animals were mosaic for a variety of insertions and deletions at each site. Strikingly, the frequencies of mutations correlated with the severities of the biomineralization defects. Almost all (33/35) sgRNA/Cas9-injected animals scored as having Severe biomineralization defects were 70 to 100% mutant at one or both sites, whereas the animals with seemingly normal skeletons had only ~3% and ~25% mutations, on average, at the sgRNA1 and sgRNA2 sites, respectively (Fig. 3*G* and Dataset S2). The radially symmetric septa produced during early skeletal deposition offered an opportunity to observe mosaic defects, and indeed we saw examples of animals with incomplete losses of biomineralized septa (*SI Appendix*, Fig. S4). These phenotypes can probably be explained by the presence of regional clones of *SLC4γ*-deficient cells surrounding the affected septa.

Discussion

Although it has been hypothesized that passive diffusion of CO_2 to the site of calcification and subsequent conversion to bicarbonate may occur (32), the requirement for SLC4γ for septum formation suggests strongly that bicarbonate transport is needed to reach the concentrations needed for calcium-carbonate deposition. Moreover, the strong phenotypes of *SLC4γ*-deficient animals also demonstrate that SLC4γ function cannot be supplied by the other *A. millepora* SLC4 family members, indicating that SLC4γ has

been specialized during evolution to play its distinctive role. This specialization presumably occurred after the coral-specific gene duplication of *SLC4β,* as indicated by the differences in *SLC4γ* and *SLC4β* expression during the onset of biomineralization in young polyps. SLC4β and SLC4γ proteins are also differentially expressed in adult *S. pistillata,* where SLC4γ is highly expressed in calicoblastic cells and SLC4β appears to be expressed ubiquitously, suggesting that their specialization of function may persist during biomineralization in adult corals (27, 32).

Although our analysis shows that the function of SLC4γ is required for calcification, the details of the bicarbonate transport remain unclear. SLC4γ is found at both the apical and basal surfaces of calicoblasts (27, 32) and may be involved in transporting bicarbonate into the calicoblasts, out of the calicoblasts to the site of calcification, or both. A goal of future research will be to answer such questions (9). For example, in future experiments, the cellular nature of the bicarbonate transport disrupted in the *SLC4γ* mutants might be determined by measuring the transport of isotope-labeled bicarbonate in wild-type and mutant polyps.

Coral species differ dramatically in skeletal morphology (37), but the molecular underpinnings of these differences are unknown. Our analyses indicate that *SLC4γ* is present in all stony corals and is required for skeleton formation in at least one complex coral, *A. millepora*. The most parsimonious explanation of these results is that SLC4γ was neofunctionalized in the last common ancestor of the stony corals to play a role in biomineralization that has since been conserved. Consistent with this interpretation, treatment with a broad-acting chemical inhibitor of bicarbonate-anion transporters reduces calcification rates in the robust coral *S. pistillata* (15, 29). However, there may be differences in the specific functions of *SLC4γ* across coral species. Indeed, other transporters associated with skeleton formation have different localization patterns in complex and robust corals (31). The striking differences between robust and complex corals in the genomic arrangement of *SLC4γ* and *SLC4β* (Fig. 1*B*) might affect the positions of these genes relative to transcriptional enhancers, topologically associated domains, and other regulatory elements, and thus affect their expression and effects on morphology (38–40). It may be possible to explore this hypothesis and whether *SLC4γ* function is conserved by comparing robust and complex coral species for *SLC4γ* expression at a single-cell level and the phenotypes associated with *SLC4γ* mutations. The stereotypical pattern of early-forming septa should allow the detection of subtle defects produced by such mutations and thus make young coral polyps a sensitive model for study of the genetic basis of biomineralization.

By coupling CRISPR/Cas9 genome editing with amplicon sequencing of individuals, we were able to directly link genotype to phenotype in individual coral animals. The extent of the correlation was remarkable, given that, in principle, an individual could have a low overall frequency of mutations but a strong phenotype, or the reverse, depending on whether the relevant clones of cells (in this case, presumably calicoblasts) carried the mutations in the mosaic animals. This study also extends the range of CRISPR/Cas9 methods for corals by demonstrating that it is possible to generate and analyze the phenotypes of mutant juveniles (and, by extension, adults). These advances should enable direct and rigorous genetic analyses of various ecologically important traits such as the determinants of algal-symbiont specificity and heat tolerance. As corals continue to decline from stressors associated with climate change, it will be particularly important to analyze the molecular mechanisms of coral stress-response pathways, including those involved in response to reactive-oxygen species (41, 42), immune stress (43, 44), and unfolded-protein stress (45, 46), all of which have been associated with the breakdown of the symbiosis during heat-induced bleaching. A more detailed understanding of the genetic basis of ecologically important traits will be valuable in developing and evaluating novel reef management and restoration strategies (47–50).

Furthermore, by combining CRISPR/Cas9-based genetic manipulations with the ability to maintain corals long-term and achieve spawning throughout the year in the laboratory (51, 52), it should be possible to initiate genetic studies throughout the year and to generate mutant coral lines, which in turn should allow at least the following: i) The long-term investigation of the cellular and developmental functions of target genes without relying on seasonal coral-spawning events. ii) The sharing of mutant lines among research groups. iii) The generation of double mutants and reporter lines through genetic crosses. These technical advances should open the way to a more rigorous understanding of coral molecular and cellular biology, which should be a vital resource in the battle to save these ecologically critical organisms from the ravages of climate change (50).

Materials and Methods

Coral Collection, Spawning, and Husbandry. *A. millepora* colonies were collected from the Great Barrier Reef (specifically Davies, John Brewer, and Falcon Island Reefs) during November 2019 and transferred to the National Sea Simulator Facility at the Australian Institute of Marine Science (AIMS), where they were kept in outdoor flow-through aquaria under ambient light and temperature conditions. Each night, the colonies were isolated in containers and allowed to spawn, which occurred on November 16, 17, and 19. Egg and sperm bundles were collected, and sperm were separated from the eggs by gently washing the bundles through a 120-μM filter. Eggs and sperm from each spawned colony were then kept separate until fertilization. Fertilizations using pooled eggs and sperm from several colonies (at a final sperm concentration of ~10^6 cells mL^{-1}) were performed at 1-h intervals for ~5 h. These staggered fertilizations provided time for microinjections to be performed before first zygotic cleavages (typically ~60 to 90 min postfertilization). Fertilized zygotes were incubated at 27 °C in filtered seawater (< 1 larva mL^{-1}) to allow further development. Zygotes from the three nights of spawning were treated as three independent replicate experiments.

Phylogenetic and Synteny Analysis of *SLC4* Genes. The phylogenetic relationships of 30 stony corals and 15 outgroups were determined using the predicted protein sequences from published reference genomes (*SI Appendix*, Table S1) and Orthofinder2 (v2.5.4) with default parameters (53) to identify orthologous gene groups ("orthogroups") across species. We searched these orthogroups for the five *S. pistillata* SLC4 proteins (32) and found that these proteins were distributed across two orthogroups containing the SLC4α-ε proteins (SLC4α-δ in one and SLC4ε in the other). In some of the genomes, several isoforms of individual SLC4 proteins are predicted. In these cases, we discarded duplicated isoforms and selected the longest protein sequence to include in the subsequent phylogenetic analysis. To build a bootstrapped phylogenetic tree of the SLC4 protein family, we generated a protein alignment using sequences from both orthogroups using MUSCLE with default parameters (v3.8.4) (54). The alignment was trimmed using TrimAl (v1.3), with the following parameters: *method* = Automated 1, *column overlap* = 0.3, *sequence overlap* = 30% (55). This alignment was then used to make a maximum-likelihood tree with 1,000 bootstraps using PhyML (v3.3.20211231) (56) with the "LG + G" substitution model determined using ProtTest3 (v.3.4.2) (57). The positions of the five *S. pistillata* SLC4 proteins and synteny across the scaffolds containing *SLC4* genes (see below) were used to identify the SLC4α-ε subfamilies in the resulting tree. All trees were visualized using Dendroscope3 v3.8.1 (58). Using this approach, SLC4γ was found in each stony-coral protein database except that for *G. fascicularis.* However, a manual BLASTn search using the *Pachyseris speciosa SLC4γ* nucleotide sequence as a query against the *G. fascicularis* genome database identified a clear SLC4γ ortholog that was not present in the predicted protein sequences (Fig. 1 *A* and *B* and Dataset S1).

To examine synteny across the genomic regions surrounding *SLC4β* and *SLC4γ*, we identified the relevant scaffolds from each cnidarian species using the genome annotation GFF files, extracted the position of each gene on these scaffolds, and identified homologous genes using the orthogroups generated by Orthofinder.

Cases in which orthologous genes were present in the same order across species were inferred to represent synteny. Orthology and synteny information for genes surrounding *SLC4β* and *SLC4γ* as used in this study is provided in Dataset S1.

Identification of *SLC4γ* in *A. millepora*. The bootstrapped phylogenetic tree of the SLC4 protein sequences (*SI Appendix*, Fig. S1) identified an apparent SLC4γ (NCBI: XP_029206541.1) in *A. millepora*. A BLASTn search using the corresponding mRNA sequence (NCBI: XM_029350708.2) as a query against the *A. millepora* genome database (59) identified a single scaffold (NCBI: NC_058076.1) containing *SLC4γ* (Dataset S1), and the alignment predicted a gene containing 14 exons spanning ~16 kb (Fig. 3*A*).

Analysis of *SLC4γ* and *SLC4β* mRNA Expression. Larvae produced on November 17 were induced to settle at 7 d postfertilization in six-well plastic plates containing 5 mL of filtered seawater per well with a chip of crustose coralline algae (CCA) of species *Porolithon onkodes*, a known inducer of *A. millepora* settlement and metamorphosis (34). The larvae generally attached by 12 h, metamorphosed by 24 h, and began biomineralization by 48 h. At each of those times, four to six individuals were preserved in 500 μL RNA*later* (Sigma no. R0901) and stored at −20 °C until further processing.

Total RNA was extracted from each individual using a modified extraction protocol (60). Briefly, each animal was transferred to a sterile 1.5-mL tube containing 100 μL TRIzol Reagent (Ambion no. 15596018) and homogenized using an RNase-free pestle. After homogenization, an additional 900 μL TRIzol and 10 μL Glycogen, RNA grade (Thermo Scientific no. R0551), were added to each tube, and the tubes were vortexed briefly and allowed to incubate at room temperature for 10 min. After adding 100 μL bromochloropropane to each tube and incubating again at room temperature for 10 min, the tubes were centrifuged at 16,000 rcf for 15 min at 4 °C. Five hundred microliters of each upper aqueous layer were transferred to a new 1.5-mL tube containing a mixture of 250 μL 100% isopropanol and 250 μL High-Salt Solution for Precipitation (Plant) (Takara Bio no. 9193) and stored overnight at −20 °C for RNA precipitation. The RNA was then pelleted at 16,000 rcf for 15 min at 4 °C, washed with 1 mL of cold 75% ethanol, and pelleted and washed again. Finally, the supernatants were removed, and the RNA pellets were allowed to air dry for 3 min before being resuspended in 50 μL nuclease-free water. Each sample of total RNA was treated with DNase and purified using a *Quick*-DNA/RNA Microprep Plus Kit (Zymo no. D7005), then eluted in 10 μL nuclease-free water.

For qRT-PCR, forward and reverse primers for *SLC4γ* and *SLC4β* were designed using Primer3Plus with default parameters (*SI Appendix*, Table S2) (61)**.** We used previously reported primers targeting the ribosomal protein L9 (*RPL9*) gene as our internal control for qRT-PCR (62). For each RNA sample, cDNA was synthesized in 10 μL reactions with 2 μL of total RNA input using the iScript cDNA Synthesis Kit (Bio-Rad no. 1708890). The resulting cDNAs were diluted to 20 ng μL^{-1} and used to amplify *SLC4γ*, *SLC4β*, and *RPL9*. qRT-PCR reactions were set up as triplicate 20 μL reactions [10 μL SsoAdvanced Universal SYBR Green Supermix (Bio-Rad no. 1725271), 0.75 μL each of forward and reverse primer at 10 μM, 4.5 μL H_2O, and 4 μL diluted cDNA] and amplified with Bio-Rad CFX 96 (one cycle at 95 °C for 30 s; 45 cycles at 95 °C for 10 s; 60 °C for 45 s; and a final melting step from 65 °C to 95 °C in 60 cycles at a rate of 0.5 °C per 5 s cycle). To calculate the relative changes in gene expression, the threshold cycles (C_T) of *SLC4γ* and *SLC4β* were first normalized to the C_T of *RPL9* ($\Delta C_T = C_{T\,[\text{target gene}]} - C_{T\,[\text{control gene}]}$). The fold changes in *SLC4γ* and *SLC4β* mRNA expression were then calculated relative to the mean *SLC4γ* expression in larvae at 0 h using the $2^{-\Delta\Delta CT}$ method (63).

Design and Synthesis of sgRNAs Targeting *SLC4γ*. The *SLC4γ* mRNA sequence was analyzed to identify good sgRNA-target sequences using a previously developed pipeline (36, 64). Briefly, all potential target sites that matched the pattern [G, C, or A]N_{20}GG were identified in the exon sequences, and all sites that had exact matches elsewhere in the *A. millepora* genome were identified using Bowtie2 (65) and removed from consideration. Potential sgRNAs with GC content >55% and those that contained polyT motifs were also removed. Next, possible sgRNA secondary structures were calculated using the Vienna RNA-fold package (66), and potential sgRNAs for which the stem-loop structure could not fold correctly for Cas9 recognition (67) were removed unless the folding energy was above −18 kcal mol^{-1}, where alternative structures would be very unstable. Next, the specificity of each potential sgRNA target was evaluated using an optimized reimplementation of the Zhang tool (68), which provides a score for the off-target risk, and targets that scored below 75 were removed from consideration. The potential sgRNA sequences that satisfied all these criteria were considered high quality and suitable for use. We then chose two sites (one in exon 5 and one in exon 10) for use based on three criteria: i) the sites are far enough downstream of the putative start of the coding sequence to avoid complications from alternative transcriptional start sites (if any); ii) the sites are far enough upstream of the putative end of the coding sequence that any frame-shifting mutations should severely truncate SLC4γ; and iii) the sites have one 5′ G, because this nucleotide is required for in vitro transcription from the T7 RNA polymerase (69, 70).

To generate DNA templates for the in vitro transcription of the sgRNAs, we added i) an 8-bp sequence at the 5′ end to facilitate RNA-polymerase binding; and ii) the T7-promoter sequence 5′ and the sgRNA-scaffold sequence 3′ to the sgRNA target sequence (*SI Appendix*, Table S2). DNA templates were synthesized using the gBlocks Gene Fragment service (IDT). Templates were reconstituted in nuclease-free H_2O to a concentration of 300 μM, and 2 μL were used directly in a 10 μL in vitro transcription reaction using the MEGAshortscript T7 Transcription Kit (Invitrogen no. AM1354). The resulting sgRNAs were purified using a Zymo RNA Clean & Concentrator 25 Kit (Zymo no. R1017). The quality and quantity of the RNA were determined using a NanoDrop spectrophotometer and gel electrophoresis.

Microinjection of sgRNA/Cas9 Complexes. sgRNA/Cas9 ribonucleoprotein complexes were generated and microinjection was performed as described previously (35, 36). Briefly, we coinjected the zygotes immediately after fertilization with a fluorescent dextran indicator [0.2 μg μL^{-1} of Alexa Fluor 488-labeled dextran (10,000 MW, Anionic, Fixable; Invitrogen no. D22910)] and either Cas9 protein alone or an equimolar mixture of the two sgRNA/Cas9 complexes. Injections were performed using a fluorescence microscope (GFP filter, excitation 488 nm) to monitor the volume injected into each zygote. We attempted to inject a volume equal to ~10% of the zygote's volume. At 12 h postfertilization, we manually sorted the zygotes into fluorescent (successfully injected) and non-fluorescent (not successfully injected) groups based on the presence of the 488-labeled dextran indicator (*SI Appendix*, Table S3) (36).

Assessment of Skeleton Formation. For each experiment, we attempted to induce settlement of both uninjected larvae and larvae injected either with Cas9 protein alone or with the sgRNA/Cas9 complexes. The settlement trials began at 5 d postfertilization in Experiments 1 and 3 and at 4 d postfertilization in Experiment 2 and involved 20–60 larvae per treatment in each experiment (*SI Appendix*, Table S4). Larvae were examined every 12 h, and animals that had not settled within 24 h were transferred to a new well with fresh seawater and a new chip of CCA. Juveniles were then imaged 3 d after settlement using a Leica MZ-FL-III inverted stereomicroscope, which allowed visualization of the sites of skeleton formation. Animals that settled in positions that prevented the imaging of their skeletons (e.g., the wall or edge of the well) were excluded from the analysis. The juveniles were also imaged using a Lecia MZ10 F upright stereomicroscope, which allowed evaluation of the presence of tentacles and a mouth. After imaging, individual animals were scraped from the well with a pipette tip and preserved in 0.5 mL of 100% ethanol until genotyping. The samples were labeled with unique identifiers that connected each tissue sample with the corresponding images.

To assess skeleton formation, the images of individual juveniles were given randomized names using a custom R script. The randomized images were then scored independently by three individuals (authors A.I.T., L.M.Y.M.-F., and P.A.C.) using the following scale: Normal, seemingly full mineralization of each visible septum; Moderate, one or two visible septa without or with incomplete mineralization; Severe, three or more septa without or with incomplete mineralization. In cases where only part of an animal was visible, it was scored as Severe only if each visible septum lacked mineralization (Fig. 3*E* and *SI Appendix*, Fig. S4).

Detection of CRISPR/Cas9-Induced Mutations by MiSeq Amplicon Sequencing. Total DNA was extracted from the ethanol-preserved juvenile tissue using a modified extraction protocol (71). Briefly, samples were pelleted by centrifugation, resuspended in 750 μL of cell-lysis buffer (100 mM Tris, pH 9.0, 100 mM NaCl, 100 mM EDTA, 1% SDS) containing 20 μL of Proteinase K (20 mg mL^{-1}; Zymo no. D3001-2-B), and incubated at 65 °C for 2 h. 187.5 μL of 5 M potassium acetate (pH 8.9) were added to each sample, and the samples were chilled on ice for 10 min. Cellular debris was removed by centrifugation at 16,100 rcf for 20 min, 800 μL of each supernatant were transferred into a new

tube, DNA was precipitated in 100% isopropanol and pelleted by centrifugation at 16,100 rcf for 15 min, and the pellets were washed with 70% ethanol and centrifuged at 16,100 rcf for 5 min. Finally, the supernatants were removed, the DNA pellets were air dried for 5 min, and the purified DNA was then resuspended in 20 µL of 10 mM Tris pH 8.5.

To generate PCR products for amplicon sequencing, we amplified 319- and 310-bp regions around exons 5 and 10, respectively (Fig. 3*A*). One microliter of genomic DNA was used in 25-µL PCR reactions using KOD HotStart DNA Polymerase (Sigma-Aldrich no. 71086) and amplicon-specific primers with Illumina overhang adapters (*SI Appendix*, Table S2). PCR cycling used the following parameters: one cycle of 95 °C for 2 min; 35 cycles of 95 °C for 20 s, 56 °C for 30 s, and 70 °C for 5 s; one cycle of 70 °C for 5 min. The PCR products were verified using gel electrophoresis, purified using a Zymo Select-a-Size DNA Clean and Concentrator Magbead Kit (Zymo no. D4085), and eluted in 53 µL of 10 mM Tris pH 8.5. Each resulting PCR product was then used in a second PCR reaction using KAPA HiFi HotStart ReadyMix (Roche Molecular Systems Inc. no. 7958935001) to add dual-index barcodes for sample multiplexing and Illumina sequencing adapters (*SI Appendix*, Table S5). PCR cycling used the following parameters: one cycle of 95 °C for 3 min; 8 cycles of 95 °C for 30 s, 55 °C for 30 s, and 72 °C for 30 s; one cycle of 72 °C for 5 min. The resulting PCR products were verified, purified, and eluted in 30 µL 10 mM Tris pH 8.5. To make a pooled sequencing library, these PCR products were normalized to a concentration of ~6 ng μL^{-1} using an Omega Equipure Magbead Kit (Omega Bio-tek no. M6445), pooled in equal volumes, and diluted to a final library concentration of 4 nM with 25% PhiX Control v3 (Illumina no. FC-110-3001). The final library was sequenced on an Illumina MiSeq System using paired-end 300-bp reads (Illumina MiSeq Reagent Kit v3; no. MS-102-3003) at the Carnegie Institution for Science.

To assess genotypes, we used the CRISPResso2 (v2.0.20b) software to quantify the number of CRISPR/Cas9-induced mutations at each sgRNA-target site (72). First, paired-end reads were demultiplexed, filtered for read quality, and aligned to reference sequences using the command *CRISPRessoBatch* and the following parameters: *quantification_window_size 10, quantification_window_center -3, min_average_read_quality 30, min_single_bp_quality 5, min_paired_end_reads_overlap 75, min_bp_quality_or_N 20, ignore_substitutions*. These parameters set the window for mutation quantification to 10 nucleotides centered on the predicted cleavage site for each sgRNA, require that paired-end reads have at least 75 bp of overlap, and set minimum single-base quality scores. As the indices were the same for both amplicons for each sample, we aligned each sample's reads to the exon 5 and 10 reference sequences to identify reads originating from each target site. All other CRISPResso2 parameters were set to default. Uninjected animals had low frequencies of polymorphisms seen at the target site (<0.1% of reads) (Dataset S1), probably resulting from rare sequencing errors during Illumina sequencing. Thus, animals with polymorphism frequencies below 0.1% were considered to have no CRISPR/Cas9-induced mutations.

Data, Materials, and Software Availability. All other data are included in the manuscript and/or supporting information. Raw sequences and metadata have been deposited in the NCBI BioProject database (accession no. PRJNA922111) (73).

ACKNOWLEDGMENTS. We thank Veronique Mocellin, Brett Baillie, and the members of the L.K.B. and Negri laboratories for valuable assistance during spawning. We also thank members of the Cleves laboratory (Natalie Swinhoe, Catherine Henderson, Ryan Hulett, and Griffin Kowalewski) and Michael Tassia for their helpful comments on the manuscript, Allison Pinder and Frederick Tan at the Carnegie Institution for Science for help with amplicon sequencing, and Manuel Aranda for helpful discussions during the project. Portions of the single-guide RNA-guide-design section were developed from the thesis of J.B. Coral collection and experimental work were conducted under Great Barrier Reef Marine Park Authority permit G11/34671.1 and AIMS Institutional Biosafety Committee approval AIMS/IBC51. This work was funded by start-up funds from the Carnegie Institution for Science (P.A.C.), an NSF-Integrative Organismal Systems (IOS) Enabling Discovery through GEnomics (EDGE) grant (2128073, P.A.C.), an International Macquarie University Research Excellence Scholarship (A.I.T.), an AIMS internal grant (L.K.B. and P.A.C.), and a Simons Foundation grant (LIFE#336932; J.R.P.)

Author affiliations: [a]Department of Embryology, Carnegie Institution for Science, Baltimore, MD 21218; [b]Applied BioSciences, Macquarie University, Sydney, NSW 2109, Australia; [c]Department of Genetics, Stanford University School of Medicine, Stanford, CA 94305; [d]Centre for Data Science, Queensland University of Technology, Brisbane, QLD 4001, Australia; [e]School of Computer Science, Queensland University of Technology, Brisbane, QLD 4001, Australia; and [f]Australian Institute of Marine Science, Townsville, QLD 4810, Australia

1. R. Fisher *et al.*, Species richness on coral reefs and the pursuit of convergent global estimates. *Curr. Biol.* **25**, 500–505 (2015).
2. J. L. Drake *et al.*, How corals made rocks through the ages. *Glob. Change Biol.* **26**, 31–53 (2020).
3. C. Simpson, W. Kiessling, H. Mewis, R. C. Baron-Szabo, J. Müller, Evolutionary diversification of reef corals: A comparison of the molecular and fossil records. *Evolution* **65**, 3274–3284 (2011).
4. T. C. LaJeunesse *et al.*, Systematic revision of Symbiodiniaceae highlights the antiquity and diversity of coral endosymbionts. *Curr. Biol.* **28**, 2570–2580 (2018).
5. J. Stanley, D. G. Fautin, Paleontology and evolution. The origins of modern corals. *Science* **291**, 1913–1914 (2001).
6. T. P. Hughes *et al.*, Spatial and temporal patterns of mass bleaching of corals in the Anthropocene. *Science* **359**, 80–83 (2018).
7. O. Hoegh-Guldberg *et al.*, Coral reefs under rapid climate change and ocean acidification. *Science* **318**, 1737–1742 (2007).
8. C. E. Cornwall *et al.*, Global declines in coral reef calcium carbonate production under ocean acidification and warming. *Proc. Natl. Acad. Sci. U.S.A.* **118**, e2015265118 (2021).
9. J. L. Drake, N. Varsano, T. Mass, Genetic basis of stony coral biomineralization: History, trends and future prospects. *J. Struct. Biol.* **213**, 107782 (2021).
10. S. Tambutté *et al.*, Coral biomineralization: From the gene to the environment. *J. Exp. Mar. Biol. Ecol.* **408**, 58–78 (2011).
11. G. C. Bourne, Memoirs: Studies on the structure and formation of the calcareous skeleton of the Anthozoa. *J. Cell. Sci.* **s2–41**, 499–547 (1899).
12. M. Tresguerres *et al.*, "Cell biology of reef-building corals: Ion transport, acid/base regulation, and energy metabolism" in *Acid-Base Balance and Nitrogen Excretion in Invertebrates*, D. Weihrauch, M. O'Donnell, Eds. (Springer, New York, 2022).
13. N. Allison, I. Cohen, A. A. Finch, J. Erez, A. W. Tudhope, Corals concentrate dissolved inorganic carbon to facilitate calcification. *Nat. Comm.* **5**, 5741 (2014).
14. D. S. Sevilgen *et al.*, Full *in vivo* characterization of carbonate chemistry at the site of calcification in corals. *Sci. Adv.* **5**, eaau744 (2019).
15. P. Furla, I. Galgani, I. Durand, D. Allemand, Sources and mechanisms of inorganic carbon transport for coral calcification and photosynthesis. *J. Exp. Biol.* **203**, 3445–3457 (2000).
16. D. Allemand *et al.*, Biomineralisation in reef-building corals: From molecular mechanisms to environmental control. *C. R. Palevol.* **3**, 453–467 (2004).
17. J. Erez, Vital effect on stable-isotope composition seen in foraminifera and coral skeletons. *Nature* **273**, 199–202 (1978).
18. A. Bertucci *et al.*, Carbonic anhydrases in anthozoan corals–A review. *Bioorg. Med. Chem.* **21**, 1437–1450 (2013).
19. W. J. Cai *et al.*, Microelectrode characterization of coral daytime interior pH and carbonate chemistry. *Nat. Comm.* **7**, 1–8 (2016).
20. A. A. Venn, C. Bernardet, A. Chabenat, É. Tambutté, S. Tambutté, Paracellular transport to the coral calcifying medium: Effects of environmental parameters. *J. Exp. Biol.* **223**, jeb227074 (2020).
21. N. Allison, I. Cohen, A. A. Finch, J. Erez, A. W. Tudhope, Corals concentrate dissolved inorganic carbon to facilitate calcification. *Nat. Comm.* **5**, 1–6 (2014).
22. S. Hohn, A. Merico, Quantifying the relative importance of transcellular and paracellular ion transports to coral polyp calcification. *Front. Earth. Sci.* **2**, 37 (2015).
23. A. C. Gagnon, J. F. Adkins, J. Erez, Seawater transport during coral biomineralization. *Earth Planet Sci. Lett.* **329–330**, 150–161 (2012).
24. J. L. Drake *et al.*, Proteomic analysis of skeletal organic matrix from the stony coral *Stylophora pistillata*. *Proc. Natl. Acad. Sci. U.S.A.* **110**, 3788–3793 (2013).
25. T. Mass *et al.*, Cloning and characterization of four novel coral acid-rich proteins that precipitate carbonates *in vitro*. *Curr. Biol.* **23**, 1126–1131 (2013).
26. D. Bhattacharya *et al.*, Comparative genomics explains the evolutionary success of reef-forming corals. *Elife* **5**, e13288 (2016).
27. X. Wang *et al.*, The evolution of calcification in reef-building corals. *Mol. Biol. Evol.* **38**, 3543–3555 (2021).
28. D. Zoccola *et al.*, Molecular cloning and localization of a PMCA P-type calcium ATPase from the coral *Stylophora pistillata*. *Biochim. Biophys. Acta.* **1663**, 117–126 (2004).
29. É. Tambutté, D. Allemand, E. Mueller, J. Jaubert, A compartmental approach to the mechanism of calcification in hermatypic corals. *J. Exp. Biol.* **199**, 1029–1041 (1996).
30. K. L. Barott, A. A. Venn, A. B. Thies, S. Tambutté, M. Tresguerres, Regulation of coral calcification by the acid-base sensing enzyme soluble adenylyl cyclase. *Biochem. Biophys. Res. Commun.* **525**, 576–580 (2020).
31. K. L. Barott, S. O. Perez, L. B. Linsmayer, M. Tresguerres, Differential localization of ion transporters suggests distinct cellular mechanisms for calcification and photosynthesis between two coral species. *Am. J. Physiol. Regul. Integr. Comp. Physiol.* **309**, R235–R246 (2015).
32. D. Zoccola *et al.*, Bicarbonate transporters in corals point towards a key step in the evolution of cnidarian calcification. *Sci. Rep.* **5**, 9983 (2015).
33. S. L. Romano, S. R. Palumbi, Evolution of Scleractinian corals inferred from molecular systematics. *Science* **271**, 640–642 (1996).
34. A. J. Heyward, A. P. Negri, Natural inducers for coral larval metamorphosis. *Coral Reefs* **18**, 273–279 (1999).
35. P. A. Cleves, M. E. Strader, L. K. Bay, J. R. Pringle, M. V. Matz, CRISPR/Cas9-mediated genome editing in a reef-building coral. *Proc. Natl. Acad. Sci. U.S.A.* **115**, 5235–5240 (2018).

36. P. A. Cleves *et al.*, Reduced thermal tolerance in a coral carrying CRISPR-induced mutations in the gene for a heat-shock transcription factor. *Proc. Nat. Acad. Sci. U.S.A.* **117**, 28899–28905 (2020).
37. J. E. N. Veron, M. G. Stafford-Smith, *Corals of the World* (Australian Institute of Marine Science, Townsville MC, Australia, 2000).
38. R. D. Acemel, I. Maeso, J. L. Gómez-Skarmeta, Topologically associated domains: A successful scaffold for the evolution of gene regulation in animals. *Dev. Biol.* **6**, e265 (2017).
39. W. de Laat, D. Duboule, Topology of mammalian developmental enhancers and their regulatory landscapes. *Nature* **502**, 499–506 (2013).
40. C. Cāestro, H. Yokoi, J. H. Postlethwait, Evolutionary developmental biology and genomics. *Nat. Rev. Genet.* **8**, 932–942 (2007).
41. M. P. Lesser, Oxidative stress causes coral bleaching during exposure to elevated temperatures. *Coral Reefs* **16**, 187–192 (1997).
42. A. C. Baker, R. Cunning, "Coral 'bleaching' as a generalized stress response to environmental disturbance" in *Diseases of Coral,* C.M. Woodley, C.A. Downs, A.W. Bruckner, J.W. Porter and S.B. Galloway, Eds. (Wiley, Hobokin, NJ, 2015), pp. 396–409.
43. K. M. Mansfield, T. D. Gilmore, Innate immunity and cnidarian-Symbiodiniaceae mutualism. *Dev. Comp. Immunol.* **90**, 199–209 (2019).
44. P. A. Cleves, C. J. Krediet, E. M. Lehnert, M. Onishi, J. R. Pringle, Insights into coral bleaching under heat stress from analysis of gene expression in a sea anemone model system. *Proc. Natl. Acad. Sci. U.S.A.* **117**, 28906–28917 (2020).
45. D. J. Barshis *et al.*, Genomic basis for coral resilience to climate change. *Proc. Natl. Acad. Sci. U.S.A.* **110**, 1387–1392 (2013).
46. N. Traylor-Knowles, N. H. Rose, E. A. Sheets, S. R. Palumbi, Early transcriptional responses during heat stress in the coral *Acropora hyacinthus*. *Biol. Bull.* **232**, 91–100 (2017).
47. S. K. Davy, D. Allemand, V. M. Weis, Cell biology of cnidarian-dinoflagellate symbiosis. *Microbiol. Mol. Biol. Rev.* **76**, 229–261 (2012).
48. V. M. Weis, S. K. Davy, O. Hoegh-Guldberg, M. Rodriguez-Lanetty, J. R. Pringle, Cell biology in model systems as the key to understanding corals. *Trends Ecol. Evol.* **23**, 369–376 (2008).
49. J. E. Parkinson *et al.*, Molecular tools for coral reef restoration: Beyond biomarker discovery. *Conserv. Lett.* **13**, e12687 (2020).
50. P. A. Cleves, "A need for reverse genetics to study coral biology and inform conservation efforts" in *Coral Reef Conservation and Restoration in the Omics Age,* M.J.H. van Oppen, M. Aranda, Eds. (Springer, New York, 2022).
51. J. Craggs *et al.*, Inducing broadcast coral spawning *ex situ*: Closed system mesocosm design and husbandry protocol. *Ecol. Evol.* **7**, 11066–11078 (2017).
52. J. Craggs, J. Guest, M. Davis, M. Sweet, Completing the life cycle of a broadcast spawning coral in a closed mesocosm. *Invertebr. Reprod. Dev.* **64**, 244–247 (2020).
53. D. M. Emms, S. Kelly, OrthoFinder: Phylogenetic orthology inference for comparative genomics. *Genome Biol.* **20**, 1–14 (2019).
54. R. C. Edgar, MUSCLE: Multiple sequence alignment with high accuracy and high throughput. *Nucleic Acids Res.* **32**, 1792–1797 (2004).
55. S. Capella-Gutiérrez, J. M. Silla-Martínez, T. Gabaldón, trimAl: A tool for automated alignment trimming in large-scale phylogenetic analyses. *Bioinformatics* **25**, 1972–1973 (2009).
56. S. Guindon *et al.*, New algorithms and methods to estimate maximum-likelihood phylogenies: Assessing the performance of PhyML 3.0. *Syst. Biol.* **59**, 307–321 (2010).
57. D. Darriba, G. L. Taboada, R. Doallo, D. Posada, ProtTest 3: Fast selection of best-fit models of protein evolution. *Bioinformatics* **27**, 1164–1165 (2011).
58. D. H. Huson, C. Scornavacca, Dendroscope 3: An interactive tool for rooted phylogenetic trees and networks. *Syst. Biol.* **61**, 1061–1067 (2012).
59. Z. L. Fuller *et al.*, Population genetics of the coral *Acropora millepora*: Toward genomic prediction of bleaching. *Science* **369**, eaba4674 (2020).
60. N. S. Walker *et al.*, Differential gene expression during substrate probing in larvae of the Caribbean coral *Porites astreoides*. *Mol. Ecol.* **28**, 4899–4913 (2019).
61. A. Untergasser *et al.*, Primer3Plus, an enhanced web interface to Primer3. *Nucleic Acids Res.* **35**, W71–W74 (2007).
62. P. Souter *et al.*, A multilocus, temperature stress-related gene expression profile assay in *Acropora millepora*, a dominant reef-building coral. *Mol. Ecol. Resour.* **11**, 328–334 (2011).
63. K. J. Livak, T. D. Schmittgen, Analysis of relative gene expression data using real-time quantitative PCR and the $2^{-\Delta\Delta CT}$ method. *Methods* **25**, 402–408 (2001).
64. G. A. Sunagawa *et al.*, Mammalian reverse genetics without crossing reveals NR3a as a short-sleeper gene. *Cell Rep.* **14**, 662–677 (2016).
65. B. Langmead, S. L. Salzberg, Fast gapped-read alignment with Bowtie 2. *Nat. Methods* **9**, 357–359 (2012).
66. R. Lorenz *et al.*, ViennaRNA Package 2.0. *Algorithms. Mol. Biol.* **6**, 26 (2011).
67. H. Nishimasu *et al.*, Crystal structure of Cas9 in complex with guide RNA and target DNA. *Cell* **156**, 935–949 (2014).
68. F. A. Ran *et al.*, Genome engineering using the CRISPR-Cas9 system. *Nat. Protoc.* **8**, 2281–2308 (2013).
69. J. Tycko, V. E. Myer, P. D. Hsu, Methods for optimizing CRISPR-Cas9 genome editing specificity. *Mol. Cell* **63**, 355–370 (2016).
70. P. I. Kulcsár *et al.*, Crossing enhanced and high fidelity SpCas9 nucleases to optimize specificity and cleavage. *Genome Biol.* **18**, 190 (2017).
71. K. Wilson *et al.*, Genetic mapping of the black tiger shrimp *Penaeus monodon* with amplified fragment length polymorphism. *Aquaculture* **204**, 297–309 (2002).
72. K. Clement *et al.*, CRISPResso2 provides accurate and rapid genome editing sequence analysis. *Nat. Biotechnol.* **37**, 224–226 (2019).
73. A. I. Tinoco *et al.*, Raw sequencing reads. *NCBI Short Read Archive*. https://www.ncbi.nlm.nih.gov/bioproject?term=PRJNA922111. Deposited 14 February 2023.